Arabian Journal for Science and Engineering (2021) 46:2663–2676
https://doi.org/10.1007/s13369-020-05185-z

RESEARCH ARTICLE-MECHANICAL ENGINEERING

Radiused Edge Blade Tip for a Wider Operating Range in Wells Turbine

P. Madhan Kumar[1] · Paresh Halder[2] · Abdus Samad[1]

Received: 21 July 2020 / Accepted: 24 November 2020 / Published online: 3 January 2021

Abstract
The narrow operating range of a Wells turbine restricts its energy extraction capability from the ocean waves. In this work, the concept of a radiused edge tip blade (RETB) was introduced to overcome such an issue. The RET modifies the tip and changes the tip leakage flow behaviour. The flow through the turbine annulus was simulated numerically and compared with the existing experimental results of the reference turbine. Three-dimensional Reynolds-averaged Navier–Stokes equations with a two-equation turbulence closure model available in ANSYS CFX 14.5 was used for the simulations. The computational domain was discretized with unstructured tetrahedral elements, and the grid independence study gave an optimal grid. The RETB altered the tip leakage flow characteristics and delayed the stall inception. The RETB enhanced the relative operating range by 25% and peak torque by 37%.

Keywords Wave energy · Wells turbine · Radiused edge tip blade · Tip leakage flow

List of Symbols

Latin

C	Chord length (mm)
Cp	Pressure coefficient (–)
e_a^{21}, e_a^{32}	Approximate relative error
e_{ext}^{21}, e_{ext}^{32}	Extrapolated relative error
$H = \frac{R_{\text{hub}}}{R_{\text{tip}}}$	Hub to tip ratio (–)
I	Turbulence intensity (–)
k	Turbulence kinetic energy (m^2/s^2)
p	Pressure (Pa)
Q	Volume flow rate (m^3/s)
y^+	Non-dimensional wall distance (–)
U_T	Peripheral blade velocity (m/s)
V_1	Absolute inlet velocity (m/s)
W_1	Relative inlet velocity (m/s)
Z	Number of blades (–)

Greek

α	Angle of attack (°)
ν	Kinematic viscosity (m^2/s)
ϕ_{ext}^{12}, ϕ_{ext}^{32}	Extrapolated values
$\in$	Turbulence dissipation rate (m^2/s^3)
$\eta = \frac{T\omega}{Q\Delta p_o}$	Efficiency (–)
ρ	Density (kg/m^3)
$\sigma = \frac{Zc}{2\pi R_{\text{mid}}}$	Solidity (–)
ω	Angular velocity (rad/s)

Abbreviations

LE	Leading edge
OWC	Oscillating water column
PS	Pressure side
RANS	Reynolds-averaged Navier–Stokes
RET	Radiused edge tip
RETB	Radiused edge tip blade
SET	Sharp edge tip blade
SS	Suction side
SST	Shear stress transport
TE	Trailing edge
TKE	Turbulence kinetic energy (m^2/s^2)
WECS	Wave energy conversion system
r	Grid refinement factor
R_{hub}	Blade hub radius (mm)
$R_{\text{mid}} = \frac{(R_{\text{tip}}+R_{\text{hub}})}{2}$	Radius of blade midspan (mm)
R_{tip}	Blade tip radius (mm)
T	Torque (N m)
$T^* = \frac{T}{\rho\omega^2 R_{\text{tip}}^5}$	Torque coefficient (–)
$U^* = \frac{U_A}{U_{\text{tip}}}$	Flow coefficient (–)
U_A	Inlet axial velocity (m/s)

✉ Abdus Samad
samad@iitm.ac.in

[1] Wave Energy and Fluids Engineering Lab, Ocean Engineering Department, IIT Madras, Chennai 600036, India

[2] Institute of Ocean Energy, Saga University, 1-Honjo-machi, Saga-shi, Saga 840-8502, Japan

U_{tip}	Blade tip velocity (m/s)
V	Absolute velocity (m/s)
w	Specific dissipation rate (s^{-1})
w_{bl}	Blade specific work (m^2/s^2)
W	Relative velocity (m/s)

1 Introduction

The ocean waves possess a huge amount of untapped energy and can be sufficient to fulfil the global energy needs. Extensive works were reported to make such energy competitive and economic [1]. Wave energy conversion system (WECS) demonstration plants and operational plants are installed in countries such as Belgium, Canada, China, Denmark, Italy, Korea, Portugal, Spain, Sweden, and the USA [2]. An oscillating water column (OWC) is a WECS that consists of a plenum chamber, entrapped air, and air turbine (Fig. 1) [3]. As the wave enters into the system or leaves the system, the OWC breathes and creates a bidirectional airflow through a duct, which rotates the turbine. Hence, for each wave cycle, the turbine faces approximately sinusoidal air velocity. The turbine has to extract energy from a wide range of flow rates for efficient operation. Hence, the efficiency of an OWC is highly dependent on turbine performance [4].

The Wells turbine used in an OWC is self-rectifying and produces unidirectional torque although the flow is bidirectional. The turbine consists of a symmetric airfoil, and the chord is aligned perpendicular to the direction of incoming flow (Fig. 1). A detailed study of the performance parameters of the Wells turbine can be found in the study by Raghunathan [5]. Several aerodynamic design modifications for Wells turbine, with guide vane and without guide vane, have been reported to improve the performance [6]. Ample efforts were made to improve the performance of the Wells turbine through various design modifications and optimization [7]. From the literature, it is found that the performance of the Wells turbine is very sensitive to tip clearance and tip leakage flow. The blade tip clearance plays a significant role in the stalling of the Wells turbine. A larger tip clearance value delays the stall and decreases efficiency. A tip clearance of less than 2%C is recommended by Watterson and Raghunathan [8] to avoid performance deterioration. Many authors adopted various methods such as endplate addition [9], tip clearance optimization [10], non-uniform tip clearance [11], duct geometry modification [12], casing treatment [13], and penetrating blade tip [14] to modify the flow characteristics of the tip leakage flow, thereby improving the performance.

The tip leakage loss is a critical factor, which affects the performance of turbomachines significantly [15–18]. There are various types of blade tip treatments like squealer tip [19, 20], radiused tip [21], contoured tip [22], and tip shape optimization [23], etc., are reported in the literature to minimize such loss. The Wells turbine is self-rectifying in nature, and its blade profiles are symmetric. Hence, the blade symmetry should be retained while adopting these tip treatments. The radiused edged tip blade (RETB) proposed by Bindon [21] mitigates the separation bubble and tip clearance losses in an annular turbine cascade [24]. The RETB streamlines the tip clearance flow and minimizes the entropy generation due to flow mixing and reattachment inside the tip clearance region

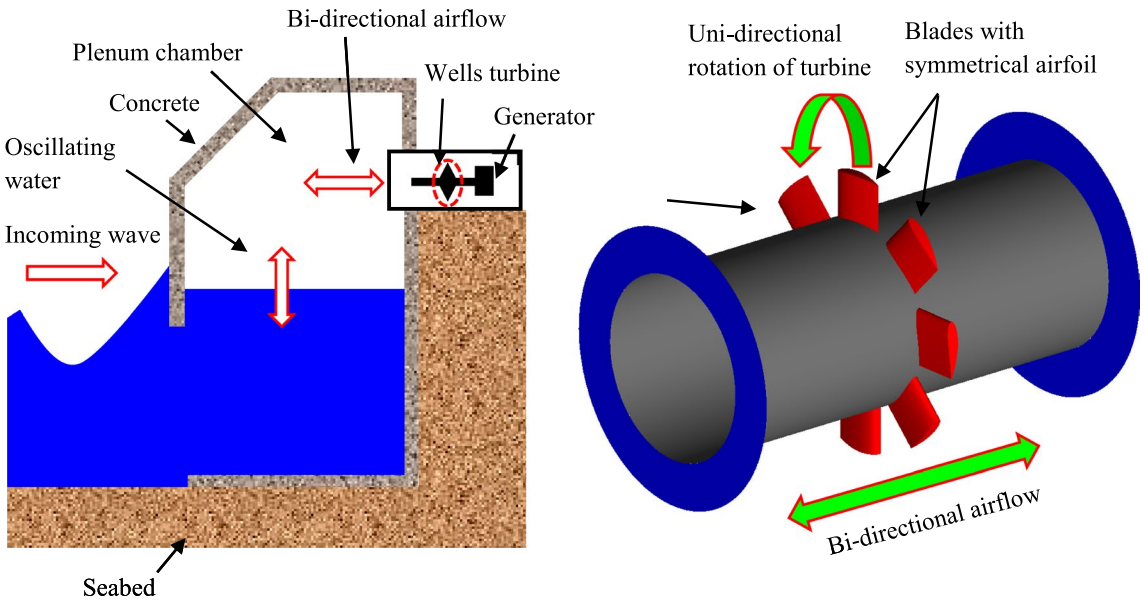

Fig. 1 Oscillating water column with Wells turbine

[22]. The RETB performs better [25–27] and minimizes the tip separation relative to a sharp-edged tip blade (SETB) [28]. The tip separation at a high flow rate gives a narrow operating range in a Wells turbine, and RETB can overcome such adverse effects. So far, no work is reported RETB used in any bidirectional flow turbines.

In the present work, the RETB concept is introduced in the Wells turbine, and the problem is solved through numerical analysis. In RETB, both sides of the blade tip edges are modified symmetrically. Different fillet radius and tip clearances are considered, and the performance is compared with the reference blade. The detailed flow analysis showing the performance change in the modified blade is reported.

Table 1 Specifications of reference geometry [10]

Blade airfoil profile	NACA 0015
No of blades	8
Chord length (C)	125 mm
Maximum thickness and its location	15%C and 30%C
Hub radius	200 mm
Tip radius	300 mm
Mean radius	250 mm
Hub to tip ratio	0.6667
Solidity at mean radius	0.64
Tip clearance	1.25 mm
Rotational speed	2000 rpm

2 Numerical Formulation

2.1 Reference Turbine

The reference Wells turbine geometry consisting of a symmetric airfoil with zero camber and untwisted blades of 90° stagger having the SET was taken from the work of Torresi et al. [10]. The design parameters are given in Table 1. The SET and RET concepts are shown in Fig. 2. The fillet created between the tip and the span of the blade has a radius of 1%C, 2%C, and 3%C. In this study, the RET was created on the suction side (SS) and the pressure side (PS).

2.2 Computational Methodology

The numerical results were obtained by solving steady Reynolds-averaged Navier–Stokes (RANS) equations in ANSYS CFX 14.5. The equations account only for the mean flow quantities without resolving the turbulent fluctuations. To resolve the closure issue, the two-equation k-ω SST turbulence model with the automatic wall function was used [29]. The k-w SST turbulence model is a hybrid model that resolves the viscous sublayer region, unlike the k-ε model which uses wall function [30]. It uses the k-w turbulence model in the viscous sublayer and the log layer region and switches to the k-ε turbulence model in the free shear flows and the wake region. It is suitable for solving flows with adverse pressure gradients and flow separation. Moreover, several researchers successfully used the k-w SST model to simulate the Wells turbine problem [13, 31, 32]. Hence, the

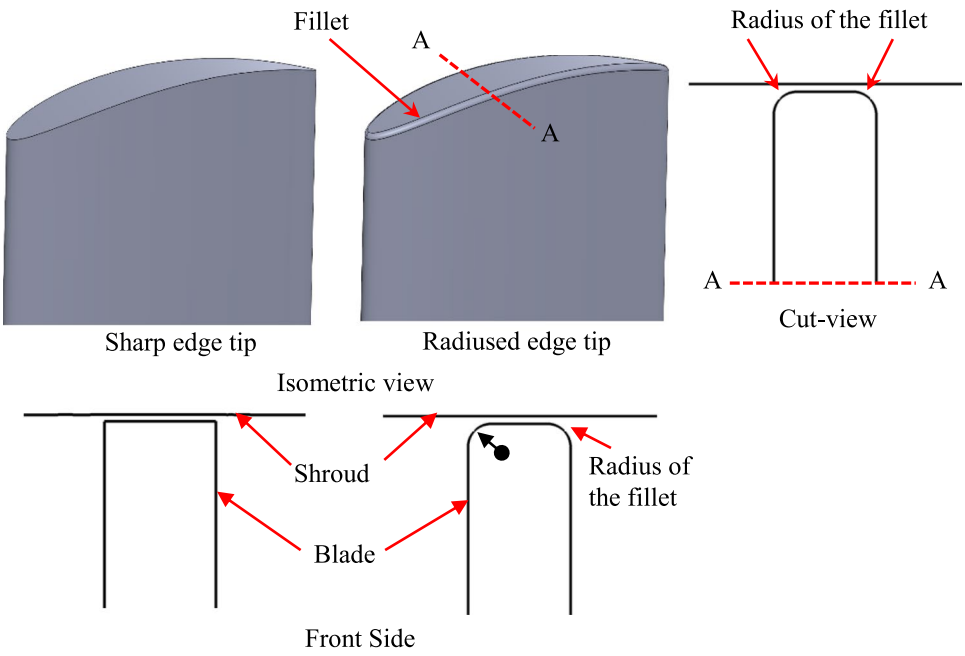

Fig. 2 Sharp edge tip and radiused edge tip blade

k-w SST model was selected as the turbulence closure model for the present study.

The turbulence kinetic energy (k) and the specific dissipation rate (w) are obtained from the subsequent transport equations [33]:

$$\rho\frac{\partial k}{\partial t}+\rho u_j\frac{\partial k}{\partial x_j}=\frac{\partial}{\partial x_j}\left[\left(\mu+\sigma*\mu_t\right)\frac{\partial k}{\partial x_j}\right]+G_k-\rho\beta*kw\quad i,j=1,3 \tag{1}$$

$$\rho\frac{\partial w}{\partial t}+\rho u_j\frac{\partial w}{\partial x_j}=\frac{\partial}{\partial x_j}\left[\left(\mu+\sigma*\mu_t\right)\frac{\partial w}{\partial x_j}\right]+\alpha G_k-\rho\beta w^2\quad i,j=1,3 \tag{2}$$

where G_k is the turbulent kinetic energy production.

Constant	σ	$\sigma*$	α	β	$\beta*$
Value	0.5	0.5	0.56	0.075	0.09

The coefficient and constant of the SST model are as follows:

$$\text{The turbulent viscosity,}\quad \mu_t=\frac{\rho a_1 k}{\max(a_1 wSF_2)} \tag{3}$$

S and F_2 indicate the magnitude of the strain rate and blending function represented by

$$F_2=\tanh(\arg_2^2)\text{ with }\arg_2=\max\left(\frac{2\sqrt{k}}{\beta' wy},\frac{500\nu}{y^2 w}\right) \tag{4}$$

All constants are calculated from the following equation:

$$\alpha=\alpha_1 F+\alpha_2(1-F) \tag{5}$$

Constant	β'	α_1	β_1	α_{k1}	σ_{w1}
Value	0.09	0.555	0.075	0.85	0.5

The continuity and momentum equations for the incompressible, steady, and isothermal fluid flow in the tensor form are given by Eqs. 1 and 2 [30].

Continuity equation

$$\frac{\delta u_i}{\delta x_i}=0 \tag{6}$$

Momentum equation

$$u_j\frac{\partial u_i}{\partial x_j}=-\frac{1}{\rho}\frac{\partial p}{\partial x_i}+\frac{\delta}{\delta x_j}\left(\gamma\frac{\delta u_i}{\delta x_j}\right) \tag{7}$$

To ensure second-order accuracy in space, the high-resolution advection scheme was used. It uses a blend factor value of 1 in the regions of low gradients maintaining second-order accuracy and a value of 0 with a first-order accuracy in the regions of high gradients to maintain robustness [30]. The residual convergence criteria for all simulations were kept as 1.0E−5. The solver uses a fully implicit discretization of the equations and employs false timestep to accelerate convergence. ANSYS CFX 14.5 is a coupled solver, and it is much robust and stable than the segregated solver [30]. The simulations were run parallel in the VIRGO supercluster available at the Indian Institute of Technology Madras. It consists of 292 compute nodes, 2 master nodes, and 4 storage nodes. Each node has 64 GB ram, and it is populated with 2 X Intel E5-2670 8 C 2.6 GHz processor. Each simulation took around 20 h to complete, and the double-precision option was enabled for all the simulations.

2.2.1 Meshing and Boundary Conditions

A single blade passage with a cyclic boundary condition was used as the computational domain (Fig. 3). The upstream and the downstream of the computational domain were extended to 4C and 6C, respectively. The *x*-, *y*-, and *z*-axes were taken as the chordwise, streamwise, and spanwise direction, respectively. The rotor rotates in a counter-clockwise direction at 2000 rpm. The Coriolis and centrifugal components were added to the governing equations while using the rotational reference frame method [34]. The discretization of the computational domain was done with unstructured tetrahedral elements. To capture the flow physics near the blade, 20 layers of prism elements were created around the blade with a layer growth ratio of 1.2 (Fig. 3). The first cell height was chosen as 0.011 mm to retain the wall $y^+<1$.

The blade, shroud, and hub were kept as no-slip walls. The inlet and the outlet were fixed as velocity inlet and pressure outlet boundary conditions, respectively. A uniform axial velocity was applied to the inlet, and the relative pressure at the outlet was fixed at 0 atm. The inlet turbulence intensity was taken as 5%. It is described as the ratio of root mean square of fluctuating velocity components (u') and an average of the mean velocity components (U). It can be expressed as

$$I=\frac{u'}{U} \tag{8}$$

$$\text{where } u'=\sqrt{\frac{1}{3}\left(u_x'^2+u_y'^2+u_z'^2\right)}$$

$$U=\sqrt{\left(\bar{u}_x^2+\bar{u}_y^2+\bar{u}_z^2\right)} \tag{9}$$

It is also known as the level or degree of turbulence. Based on the details available in the open literature, the inlet turbulence value was fixed as 5% [5, 35, 36]. Moreover, the lateral side of the computational domain was given periodic boundary condition, to realize the periodic nature of the rotor geometry. The computational domain chosen for the flow analysis is illustrated in Fig. 4.

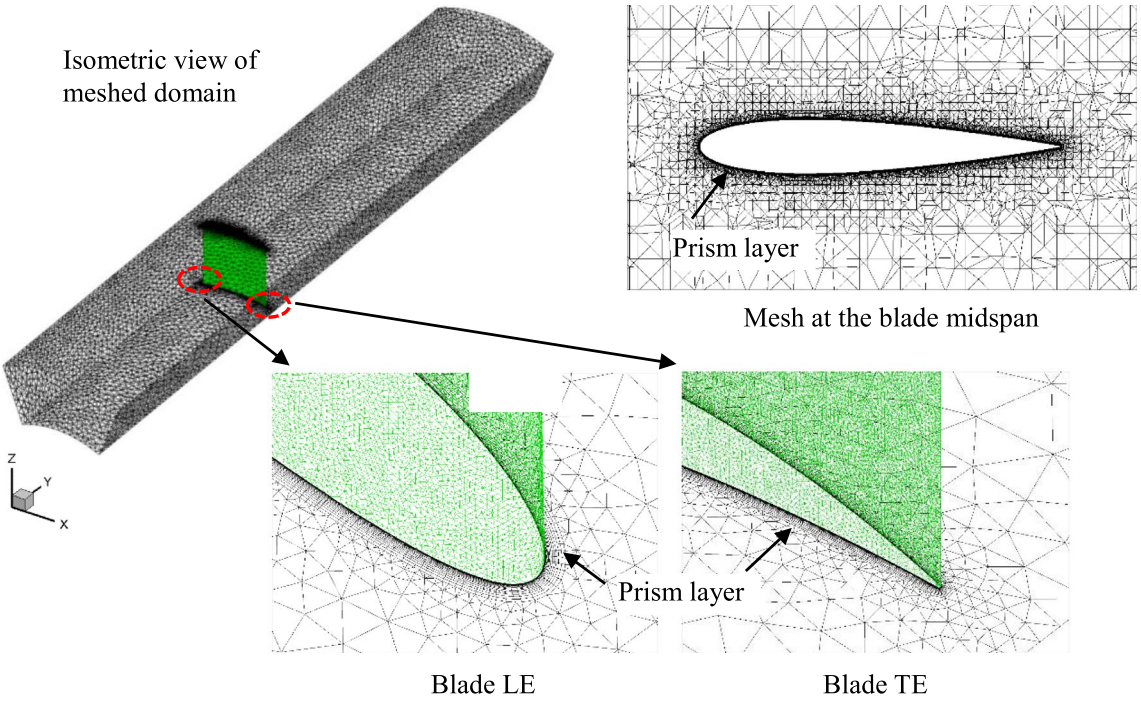

Fig. 3 Discretized computational domain

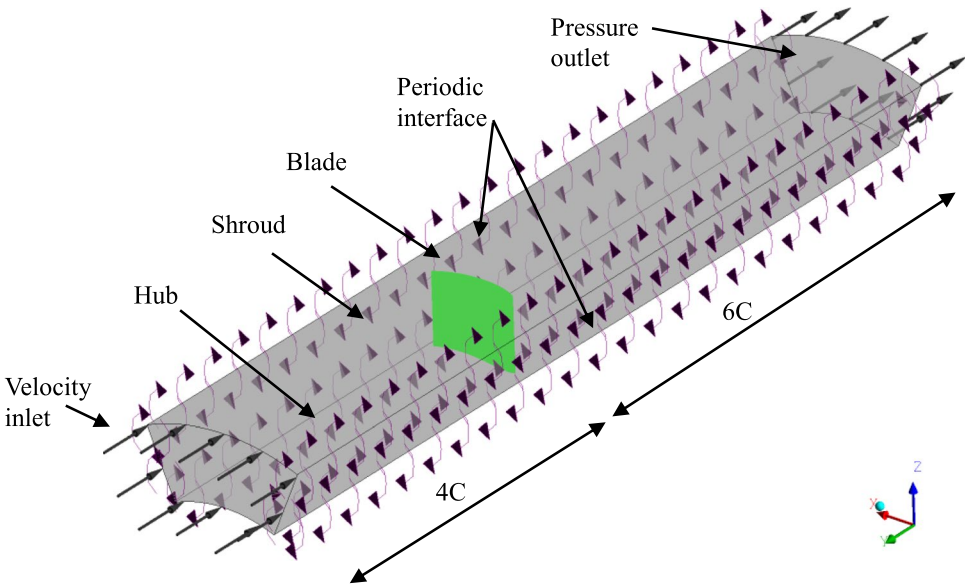

Fig. 4 Computational domain for the flow analysis

2.3 Performance Parameters of the Wells Turbine

The performance of the Wells turbine is evaluated in terms of the following non-dimensional parameters. They are listed below [10].

- Flow coefficient (U^*)

$$U^* = \frac{U_A}{U_{\text{tip}}} \tag{10}$$

where U_A is the inlet axial velocity (m/s) and U_{tip} is the blade tip velocity (m/s).

- Torque coefficient (T^*)

$$T^* = \frac{T}{\rho\omega^3 R_{tip}^5} \tag{11}$$

where T is the torque, ρ is the air density (1.225 kg/m^3), ω is the angular velocity (209.44 rad/s), and R_{tip} is the blade tip radius (m).

- Pressure drop coefficient (Δp^*)

$$\Delta p^* = \frac{\Delta p}{\rho\omega^2 R_{tip}^2} \tag{12}$$

where Δp is the pressure drop across the inlet and outlet (N/m^2).

- Efficiency (η)

$$\eta = \frac{T\omega}{Q\Delta p} \tag{13}$$

where Q is the volume flow rate of air (m^3/s).

2.4 Grid dependency and Numerical Validation

The grid convergence was assessed based on the grid convergence index (GCI). The GCI provides the uncertainty caused due to the discretization error. Three grids with a different resolution such as fine, medium, and coarse were selected with a grid refinement ratio of 1.3. The method recommended by Celik et al. [37] was used to calculate the GCI. Table 2 provides the GCI calculation result. It shows that the numerical uncertainty reduces with an increase in grid refinement. The GCI value for the fine and medium grid is 0.438% and 1.928%, respectively. According to Manna et al. [38], the grid is assumed to be spatially converged if the GCI between the successive grids is less than 3%. Hence, the medium grid with 3 million cells was retained for further simulations to reduce the computational cost, which is shown in Fig. 5. Also, to validate the present numerical results, the computations were performed for a wide flow coefficient and compared against the available experimental [39] and numerical results [10, 12, 40] (Fig. 6). The present results follow a similar trend with the existing results. The

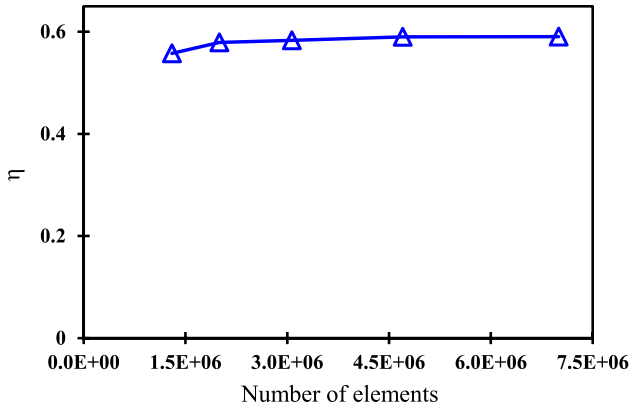

Fig. 5 Grid independency test

sudden drop in torque and the efficiency at a flow coefficient (U^*) of 0.225 indicates stall.

3 Results and Discussion

3.1 Effect of Radius Edge Tip (RET)

To evaluate the effect of RET, three fillet radii (1%C, 2%C, and 3%C) were chosen, and the results are presented in Fig. 7. As the flow coefficient increases, the torque increases up to the stall point and then falls. At a low U^*, the RET produces a lower torque. However, a higher U^* generates a higher torque, while SET blade stalls ($U^*=0.225$). On the other hand, a marginal difference in torque is observed between the performance characteristics of the RET blades with different fillet radius. The pressure drop coefficient exhibits a linear relationship with the U^*, which is a similar trend reported in the other literature [39]. The RET blade has a lower pressure drop compared to the SET blade. The efficiency of the SET blade drops rapidly at $U^*=0.225$, while the RET blade gives the efficiency drop at $U^*=0.28$. In the RET blade, the peak efficiency is lower, but RET with 1%C shows a better efficiency for the entire flow range. The

Table 2 GCI calculation

Number of cells (10^6)	Fine, medium, and coarse	6.80, 3.07, 1.39
Average cell size (h)	h_1, h_2, h_3	0.00143, 0.00186, 0.00243
Grid refinement factor (r)	r_{21}, r_{32}	1.3, 1.3
Performance parameter (ϕ)	ϕ_1, ϕ_2, ϕ_3	0.0427, 0.0422, 0.0402
Apparent order	p	5.47
Approximate relative error (%)	e_a^{21}, e_a^{32}	1.146, 4.953
Extrapolated values	ϕ_{ext}^{12}, ϕ_{ext}^{32}	0.04294, 0.04295
Extrapolated relative error (%)	e_{ext}^{21}, e_{ext}^{32}	0.349, 1.519
GCI (%)	GCI_{fine}^{21}, GCI_{medium}^{32}	0.438, 1.928

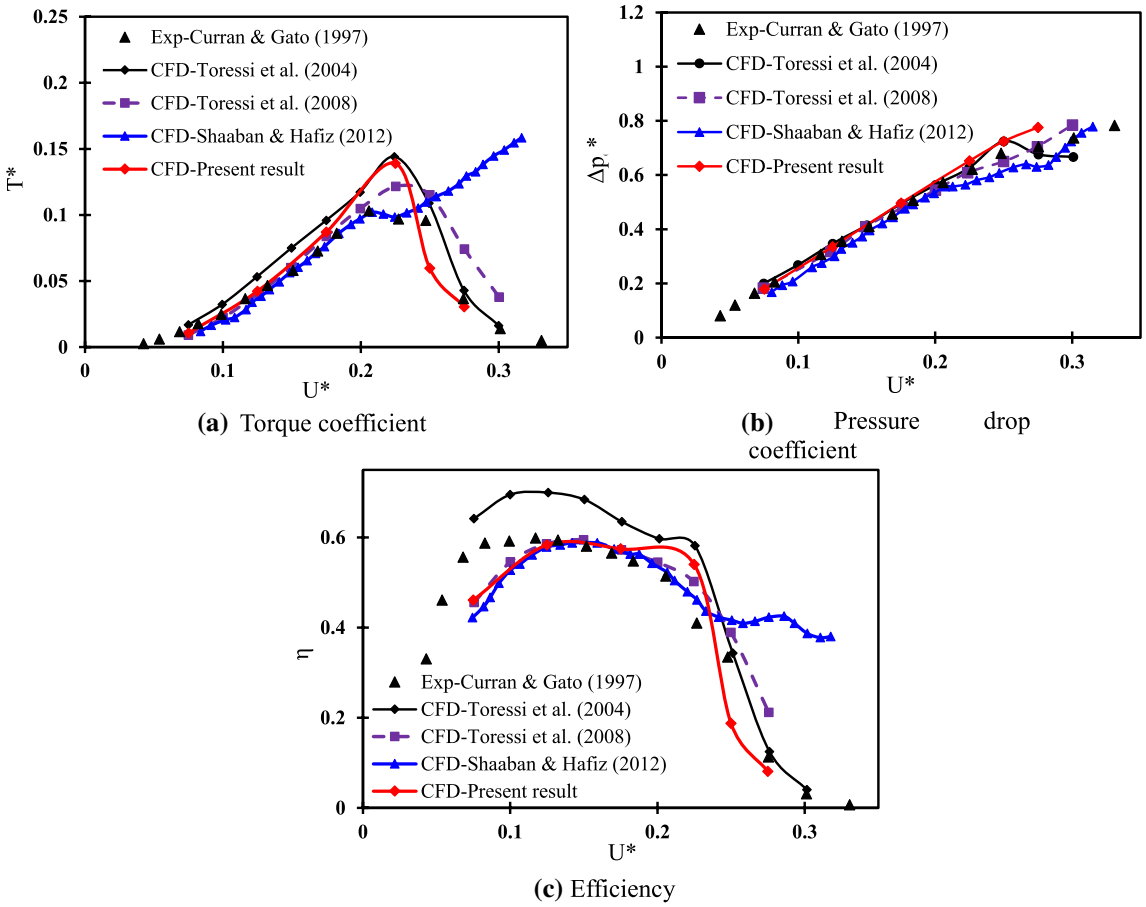

Fig. 6 Numerical validation

reduced peak efficiency can be attributed to the enlarged tip clearance causing an increase in leakage losses.

Figure 8 shows the blade loading distribution at midspan (50%) and tip (95%). As apparent, the RET blades show reduced blade loading at midspan and tip compared to the SET blade. The area of the pressure coefficient (Cp) indicates the lift force; it explains the reduced torque of RET blades at low U^*. Similar behaviour is observed at U^* 0.225, where the SET shows higher blade loading in contrast to RET blades. At high U^* (=0.275), the leading edge (LE) minimum suction pressure vanishes in the SET blade and exhibits almost constant SS pressure along the chord that indicates stall. However, the RET blade displays increased LE suction pressure and it is the reason behind the delayed stall and improved torque at higher U^*. Hence, it can be concluded that the RET blade reduces blade loading and delays the stall. Figure 9 illustrates the spanwise tangential velocity distribution along with blade LE. The tangential velocity component is related to torque generation. As evident in the figure, the tangential velocity increases from hub to tip for all cases. At $U^*=0.075$, the SET blade shows relatively higher tangential velocity compared to RET blades and it is in agreement with the results shown in Fig. 6a. The tangential velocity increases with increasing U^*. At $U^*=0.275$, the RET blade shows reduced tangential velocity near the tip that implies stall, whereas the RET blades show increased tangential velocity and delayed stall. Also, the RET blades exhibit similar performance for varying fillet radius.

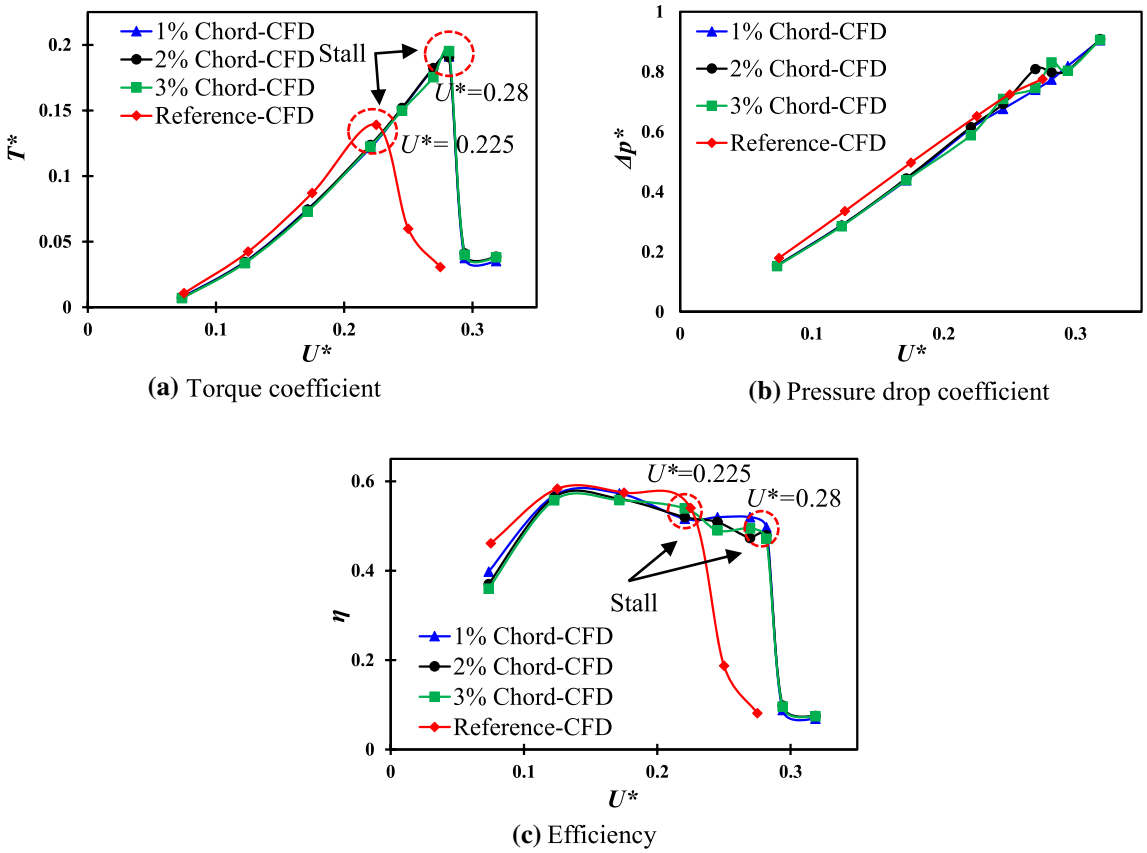

Fig. 7 Performance comparison of sharp edge and the radius edge tip blades

The inlet velocity triangle for different axial velocities is shown in Fig. 10. The terms V_1, W_1, and U_T denote absolute inlet, relative inlet, and peripheral blade velocities, respectively. The term α_1 denotes the angle of attack at the inlet, where the relative flow meets the rotating blade. The angle of attack is a critical factor that affects the stall characteristics and torque generated by the turbine.

In general, the torque increases with angle of attack up to a critical value and then decreases due to the blade stall phenomenon. Additionally, as shown in Fig. 10, for a given blade velocity, the angle of attack increases with an increase in axial velocity ($V_{1b} > V_{1a}$; $\alpha_{1b} > \alpha_{1a}$). The normalized spanwise distribution of the axial velocity near blade LE is shown in Fig. 11. It can be seen that the axial velocity of the SETB along the span is relatively higher than the RETBs. As explained earlier, reduced axial velocity decreases the angle of attack and it is responsible for the reduced torque at low U^* and the delayed stall. The SETB stalls at $U^* = 0.275$ and it shows a higher axial velocity near the tip compared to the RETBs. The reduced blade loading in the case of the RETBs (Fig. 8) is attributed to the decreased axial velocity, and it is responsible for the delayed stall and shift in peak torque towards a higher U^*.

The pressure variation between the PS and SS of the blade tip drives the tip leakage flow. It interacts with the primary flow and increases the secondary losses, which leads to reduced efficiency. It was reported in the literature that the tip leakage flow affects the performance of the Wells turbine significantly [5] [11]. The effect of the radius on the tip leakage flow is analysed using Fig. 12b. The strength of tip leakage flow is minimum at low U^* ($U^* = 0.075$), and it is predominant near the TE for all cases. The fillet radius increases the leakage flow in the RET blade. The RET blade shows higher leakage flow at low U^* compared to the SET blades, and this explains the improved efficiency of the SET blade at low U^*. With the increasing flow rate, the tip leakage flow increases for all cases.

At a higher U^*, the tip leakage flow shifts towards the LE and rolled into a vortex and interacts strongly with the primary flow, unlike the previous cases ($U^* = 0.075$ and 0.225),

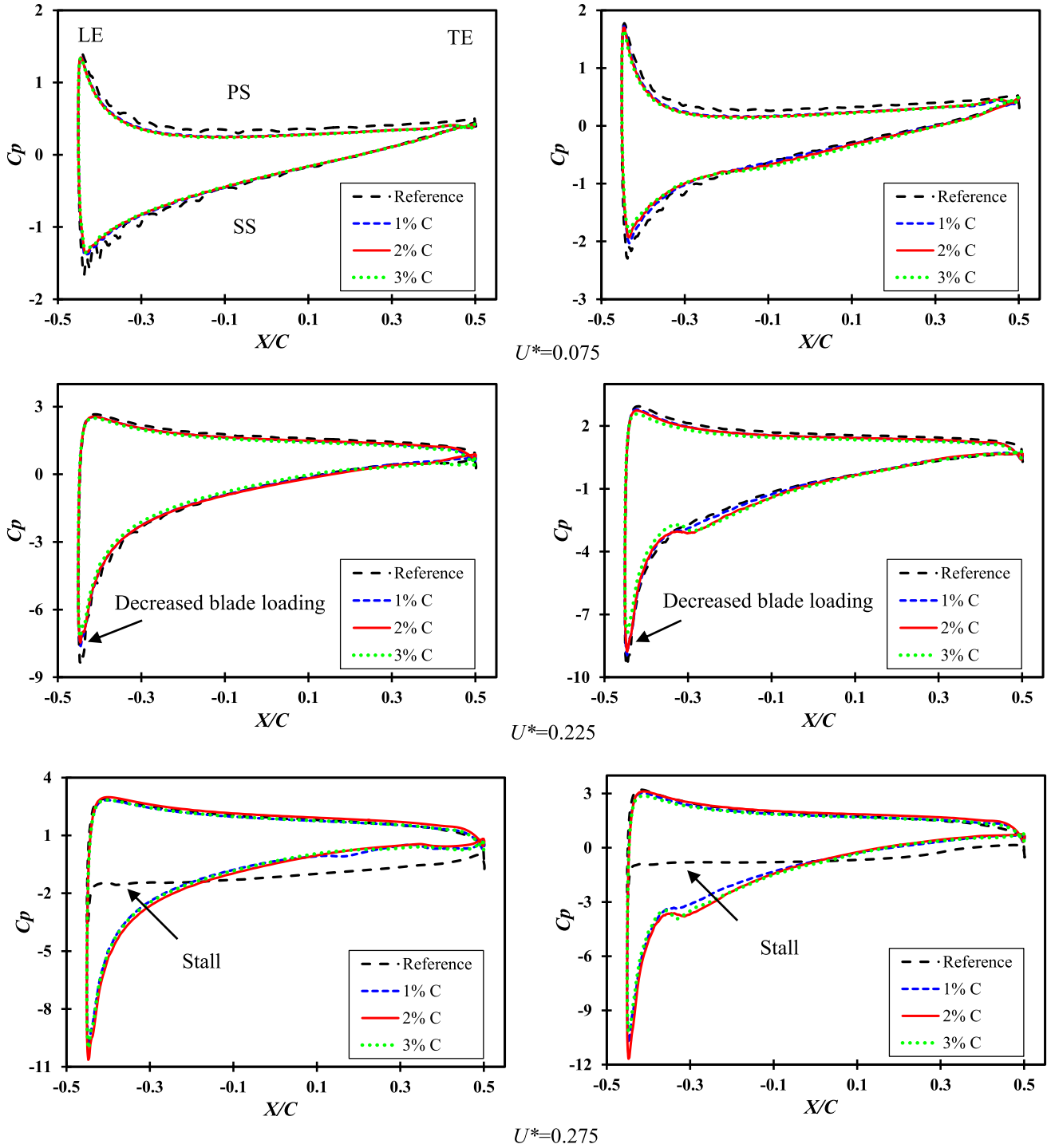

Fig. 8 Blade loading at midspan (left) and tip (right) for different U^*

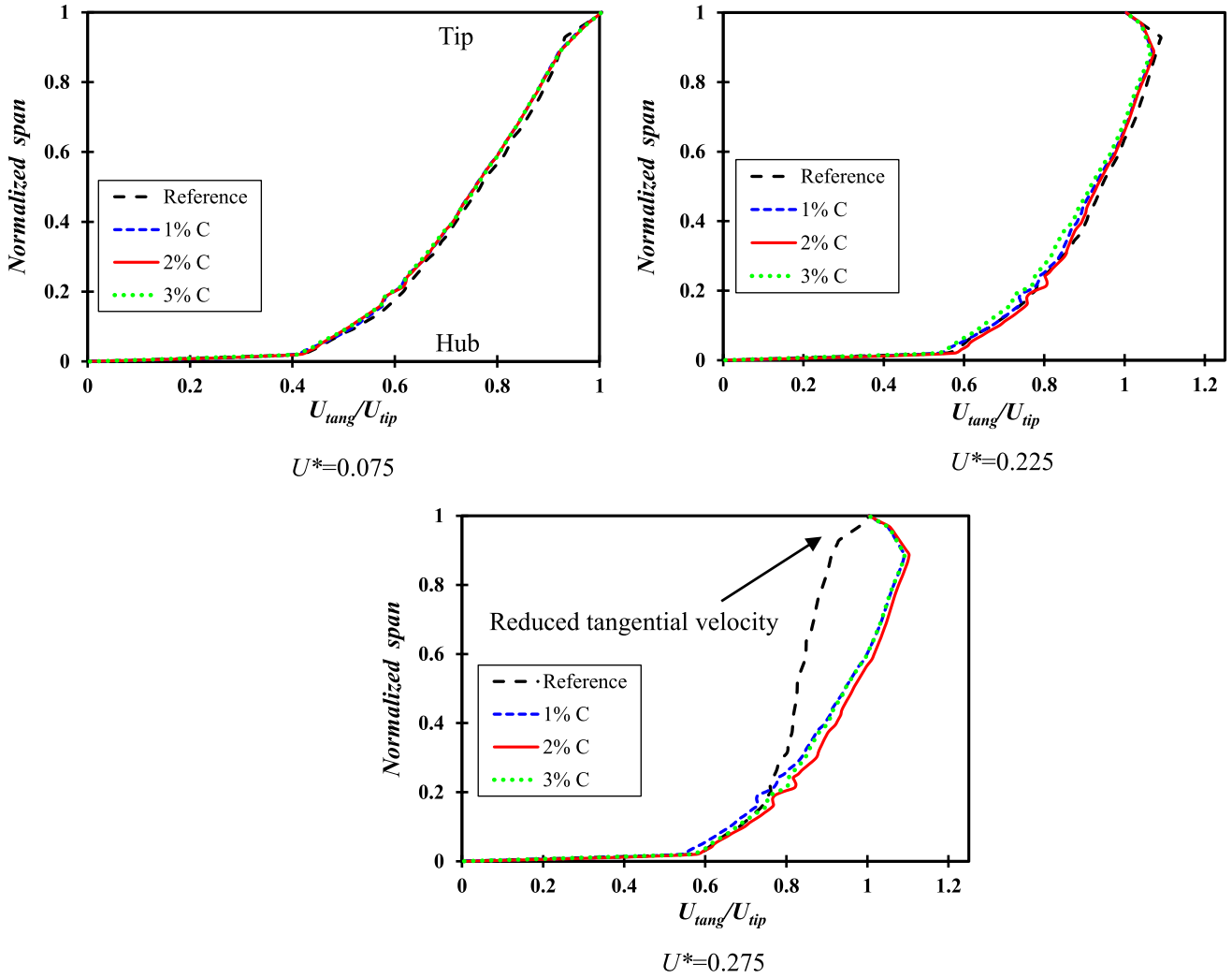

Fig. 9 Spanwise tangential velocity distribution near blade LE

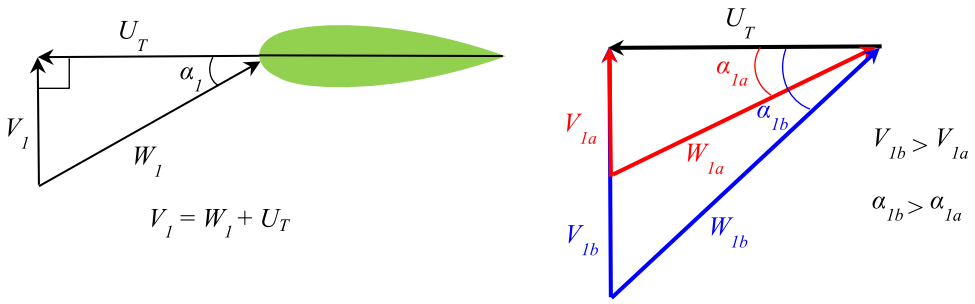

Fig. 10 Velocity triangle at inlet for different axial velocities (V_{1a} and V_{1b})

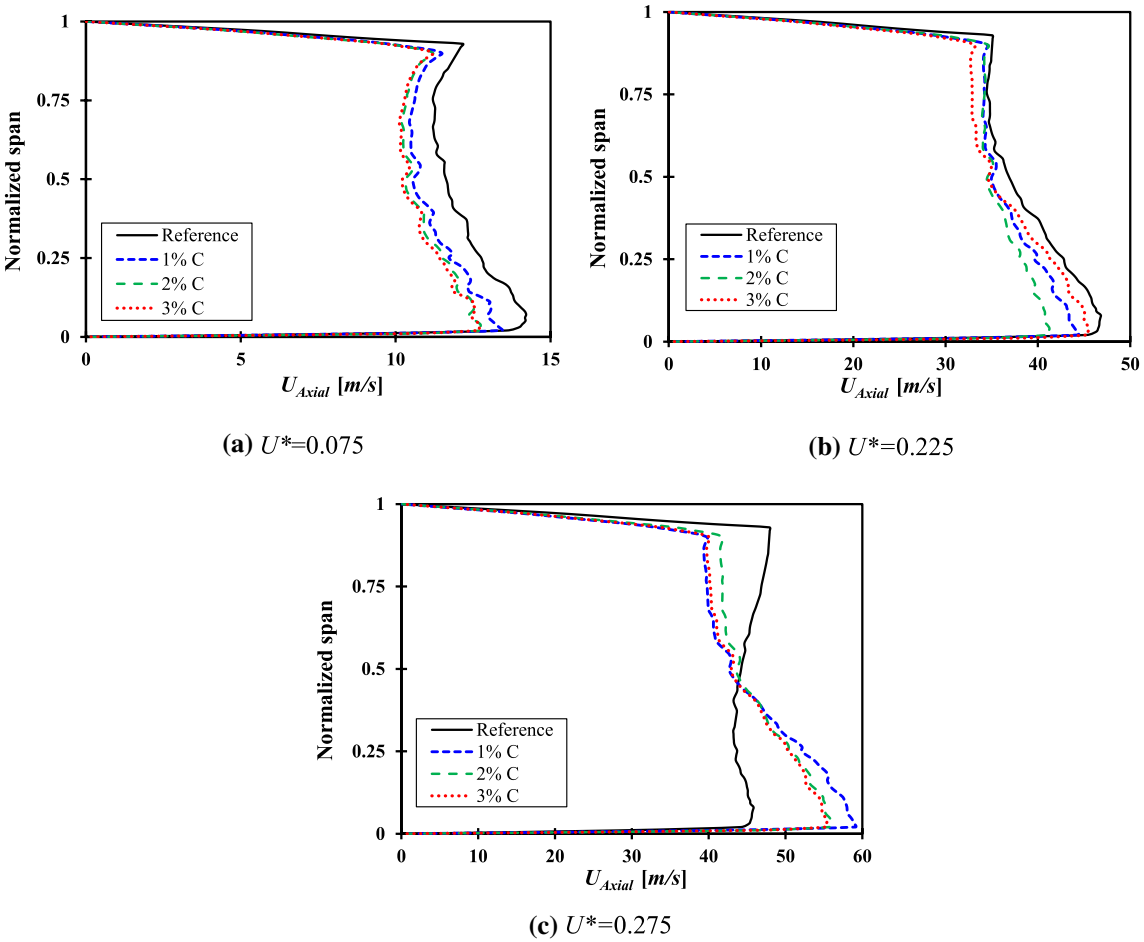

Fig. 11 Spanwise distribution of axial velocity near blade LE, for different values of U^*

where the interaction is weak. This leads to the turbine stall, and a similar phenomenon was reported by Dhanasekaran and Govardhan [41]. Moreover, the tip leakage flow emerges as a flat jet [26] in the RET blade and has a weak interaction with the primary flow even at higher U^*. On the contrary, it is rolled into a sheet of vortex in the SET blade and interacts strongly with the primary flow. The reason behind the delayed stall of the RET blades can be attributed to a weak interaction between the primary and the tip leakage flow. The delay of stall inception improved the performance of RET blades significantly at a higher U^*. Also, with an increase in fillet radius, a decrement in peak efficiency is observed.

4 Conclusions

The effect of the radiused edge tip blade on the performance of the Wells turbine is presented in this work. The numerical investigations were conducted for the entire flow range including the post-stall regime. Based on the analysis, the following conclusions were drawn.

- The radiused edge tip blades exhibit reduced blade loading at midspan and tip compared to the reference blade. The reduced blade tip loading implies reduced axial velocity and angle of attack at the tip, and it is responsible for the delayed stall and shift in peak torque towards a higher flow coefficient.
- The radiused edge tip blades showed a weak interaction between the primary and the tip leakage flow compared to the reference blade, at higher flow coefficients and improved the performance.
- The peak efficiency was reduced, and the stall point was shifted towards the higher flow coefficient.
- A marginal difference in performance is observed for radiused edge tip blades with different fillet radius.
- The radius edge blade tip showed a better performance compared to the sharp edge blade. The relative peak torque was improved by 37%, and the relative stall margin was enhanced by 25%.

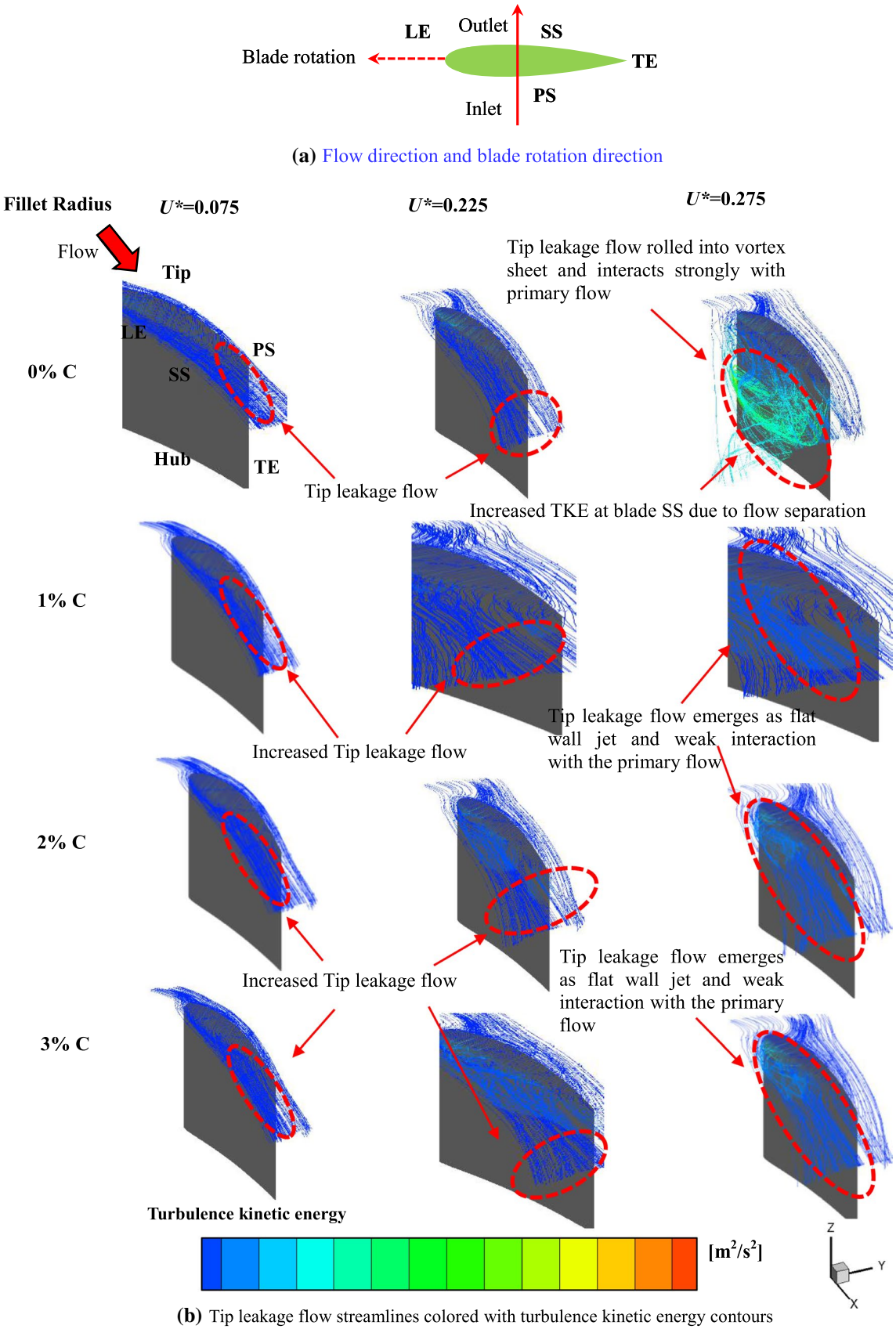

(a) Flow direction and blade rotation direction

(b) Tip leakage flow streamlines colored with turbulence kinetic energy contours

Fig. 12 **a** Flow direction and blade rotation direction. **b** Tip leakage flow streamlines coloured with turbulence kinetic energy contours

Acknowledgements The high-speed computing facility provided by the Indian Institute of Technology Madras was gratefully acknowledged.

Compliance with Ethical Standards

Conflict of interest The authors declare that they have no conflict of interest.

References

1. Mustapa, M.A.; Yaakob, O.B.; Ahmed, Y.M.; Rheem, C.K.; Koh, K.K.; Adnan, F.A.: Wave energy device and breakwater integration: a review. Renew. Sustain. Energy Rev. **77**, 43–58 (2017)
2. Brito, E.; Melo, A.; Villate, JL.: Annual report 2016. Ocean energy systems. IEA-OES, 2017
3. Falnes, J.: Ocean Waves and Oscillating Systems: Linear Interactions Including Wave-Energy Extraction. Cambridge University Press, Cambridge (2002)
4. Falcão, A.F.O.; Henriques, J.C.C.: Oscillating-water-column wave energy converters and air turbines: a review. Renew. Energy **85**, 1391–1424 (2016)
5. Raghunathan, S.: The Wells air turbine for wave energy conversion. Prog. Aerosp. Sci. **31**, 335–386 (1995)
6. Brito-Melo, A.; Gato, L.M.C.; Sarmento, A.J.N.A.: Analysis of Wells turbine design parameters by numerical simulation of the OWC performance. Ocean Eng. **29**, 1463–1477 (2002)
7. Shehata, A.S.; Xiao, Q.; Saqr, K.M.; Alexander, D.: Wells turbine for wave energy conversion: a review. Int. J. Energy Res. **41**, 6–38 (2017)
8. Watterson, J.; Raghunathan, S.: Computed effects of tip clearance on Wells turbine performance. In 35th Aerospace Sciences Meeting and Exhibit AIAA Paper 97-0994, 1997.
9. Takao, M.; Setoguchi, T.; Kinoue, Y.; Kaneko, K.: Wells turbine with end plates for wave energy conversion. Ocean Eng. **34**, 1790–1795 (2007)
10. Torresi, M.; Camporeale, S.M.; Strippoli, P.D.; Pascazio, G.: Accurate numerical simulation of a high solidity Wells turbine. Renew. Energy **33**, 735–747 (2008)
11. Taha, Z.; Sugiyono, Tuan, Ya.; TMYS.; Sawada, T.: Numerical investigation on the performance of Wells turbine with non-uniform tip clearance for wave energy conversion. Appl. Ocean Res. **33**, 321–31 (2011)
12. Shaaban, S.; Hafiz, A.A.: Effect of duct geometry on Wells turbine performance. Energy Convers. Manag. **61**, 51–58 (2012)
13. Halder, P.; Samad, A.; Kim, J.H.; Choi, Y.S.: High performance ocean energy harvesting turbine design—a new casing treatment scheme. Energy **86**, 219–231 (2015)
14. Cui, Y.; Hyun, B.S.: Numerical study on Wells turbine with penetrating blade tip treatments for wave energy conversion. Int. J. Naval Archit. Ocean Eng. **8**, 456–465 (2016)
15. Booth, T.C.; Dodge, P.R.; Hepworth, H.K.: Rotor-tip leakage: part I — basic methodology. J. Eng. Power **104**, 154–161 (1982)
16. Bindon, J.P.: The measurement and formation of tip clearance loss. J. Turbomach. **111**, 257–263 (1989)
17. Denton, J.D.: Loss mechanisms in turbomachines. In ASME International Gas Turbine and Aeroengine Congress and Exposition, ASME 93-GT-435, 1993.
18. Inoue, M.; Furukawa, M.: Physics of tip clearance flow in turbomachinery (Keynote paper). In: ASME Joint US-European Fluids Engineering Division Conference, pp. 777–789 (2002)
19. Key, N.L.; Arts, T.: Comparison of turbine tip leakage flow for flat tip and squealer tip geometries at high-speed conditions. J. Turbomach. **128**, 213–220 (2006)
20. Li, W.; Qiao, W.Y.; Xu, K.F.; Luo, H.L.: Numerical simulation of tip clearance flow passive control in axial turbine. J. Therm. Sci. **17**, 147–155 (2008)
21. Bindon, J.P.: Pressure distributions in the tip clearance region of an unshrouded axial turbine as affecting the problem of tip burnout. In: ASME International Gas Turbine Conference and Exhibition: ASME 87-GT-230 (1987)
22. Bindon, J.P.; Morphis, G.: The development of axial turbine leakage loss for two profiled tip geometries using linear cascade data. J. Turbomach. **114**, 198–203 (1992)
23. De, M.C.; Lavagnoli, S.; Paniagua, G.: Blade tip shape optimization for enhanced turbine aerothermal performance. In: ASME Turbo Expo Turbine Technical Conference and Exposition: ASME GT2013-94754 (2013)
24. Morphis, G.; Bindon, J.P. (1988) The effects of relative motion, blade edge radius and gap size on the blade tip pressure distribution in an annular turbine cascade with clearance. In: ASME International Gas Turbine and Aeroengine Congress and Exposition: ASME 88-GT-256
25. Bindon, J.P.: The microflows within the tip clearance gap of an unshrouded axial turbine and their effects on loss development. Int. J. Turbo Jet Eng. **8**, 55–74 (1991)
26. Morphis, G.; Bindon, J.P.: The performance of a low speed one and a half stage axial turbine with varying rotor tip clearance and tip gap geometry. In: ASME International Gas Turbine and Aeroengine Congress and Exposition: ASME 94-GT-481 (1994)
27. Kaiser, I.; Bindon, J.P.: The effect of tip clearance on the development of loss behind a rotor and a subsequent nozzle. In: ASME International Gas Turbine and Aeroengine Congress and Exposition: ASME 97-GT-053 (1997)
28. Ameri, A.A.; Bunker, R.S.: Heat transfer and flow on the first stage blade tip of a power generation gas turbine: part 2-Simulation results. In: ASME International Gas Turbine and Aeroengine Congress and Exposition: ASME 99-GT-283 (1999)
29. Menter, F.R.: Two-equation eddy-viscosity turbulence models for engineering applications. AIAA J. **32**, 1598–1605 (1994)
30. CFX, ANSYS.: Solver theory guide. Ansys. Inc., Canonsburg (2011)
31. Nazeryan, M.; Lakzian, E.: Detailed entropy generation analysis of a Wells turbine using the variation of the blade thickness. Energy **143**, 385–405 (2018)
32. Gratton, T.; Ghisu, T.; Parks, G.; Cambuli, F.; Puddu, P.: Optimization of blade profiles for the Wells turbine. Ocean Eng. **169**, 202–214 (2018)
33. Wilcox, D.C.: Turbulence Modeling for CFD. DCW industries, La Canada (1998)
34. ANSYS.: CFX-Solver modelling guide–Release 15.0 (2014)
35. Raghunathan, S.; Setoguchi, T.; Kaneko, K.: The effect of inlet conditions on the performance of Wells turbine. J. Energy Resources Technol. **111**(1), 37–42 (1989). https://doi.org/10.1115/1.3231399
36. Kumar, P.M.; Samad, A.: Effect of turbulence intensity on the performance characteristics of large-scale wells turbine. In: The 4th Asian Wave and Tidal Energy Conference, September (2018)
37. Celik, I.B.; Ghia, U.; Roache, P.J.; Freitas, C.J.; Coleman, H.; Raad, P.E.: Procedure for estimation and reporting of uncertainty due to discretization in CFD applications. J. Fluids Eng. **130**(7), 078001 (2008). https://doi.org/10.1115/1.2960953
38. Manna, P.; Dharavath, M.; Sinha, P.K.; Chakraborty, D.: Optimization of a flight-worthy scramjet combustor through CFD. Aerosp. Sci. Technol. **27**, 138–146 (2013)

39. Curran, R.; Gato, L.M.C.: The energy conversion performance of several types of Wells turbine designs. Proc. Inst. Mech. Eng. Part A J. Power Energy **211**, 133–145 (2005)
40. Torresi, M.; Camporeale, S.M.; Pascazio, G.: Fluid dynamic analysis low solidity Wells turbine. In: 59 congresso ATI; Genova, Italy, pp. 277–88 (2004)
41. Dhanasekaran, T.S.; Govardhan, M.: Computational analysis of performance and flow investigation on wells turbine for wave energy conversion. Renew. Energy **30**, 2129–2147 (2005)